JOURNAL OF SPACECRAFT AND ROCKETS
Vol. 36, No. 5, September–October 1999

Paraboloidally Shaped Antenna Possessing Pointing and Beam-Width Control

Robert J. Stanley* and Larry M. Silverberg†
North Carolina State University, Raleigh, North Carolina 27695-7910

The surface shape of a paraboloidal reflector was reconfigured using electrostatic forces of repulsion. The experiment consisted of a reconfigurable electrostatically shaped reflector and a measurement system. A set of test cases demonstrated pointing and beam-width control of the radiating surface. The surface reflector angles of rotation θ_x and θ_y were plotted vs eight test cases. The resulting sine functions show the near-linear relationship between voltage and pointing, indicating that expected rotations are in agreement with measurements and that a simple interpretation of Coulomb's law dominates the behavior of the system.

Nomenclature

$\boldsymbol{a}$	= vector of undetermined coefficients
$\boldsymbol{C}$	= coefficient matrix
E_x	= error function for rotation about the x axis
E_y	= error function for rotation about the y axis
i, j, k	= counting indices
p	= number of sample points in one quadrant
$\boldsymbol{R}_x, \boldsymbol{R}_y$	= rotation matrices
x_n, y_n, z_n	= coordinates in a new reference frame
z	= vertical position of ith point in the (j, k)th quadrant
$\boldsymbol{z}$	= new vertical position of ith point in the (j, k)th quadrant
$\boldsymbol{z}$	= vector of measured displacements
$z(x, y)$	= function to be curve fitted
θ_x	= angle of rotation about the x axis
θ_y	= angle of rotation about the y axis

Introduction

CURRENTLY, most space-based antennas are nonreconfigurable. The few antennas that are reconfigurable (phased array) exhibit heat rejection problems and are difficult to manufacture. Electrostatic antennas do not exhibit these problems. Reconfigurability allows the satellite antenna beam to be refocused and repointed and to scan. Applications are power maximization (in cases were the antenna experiences prohibitively large thermally induced surface deflections and transient atmospheric disturbances), mapping, and surveillance. The concept of controlling a surface with electrostatic forces was investigated in the early 1980s. These studies were constrained by material selection and hardware selection, such as power supplies and control equipment.

A parabolic cylinder reflector surface was reconfigured by modal control both theoretically and experimentally in previous work[1–3] (Fig. 1). The work presented here extends the previous work by applying the same principles to a paraboloidally shaped reflector surface. In particular, the experimental results demonstrate the antenna's ability to point in eight different directions and to bend about two different lines. General background information about adaptively configured antennas is given in Refs. 1–3.

Experimental Setup

The setup consists of two main parts: a paraboloidally shaped reflector and a cylindrical measurement device suspended above it (Fig. 2). The components of the reflector are shown in Figs. 3–5 and the components of the cylindrical measurement device are shown in Figs. 6 and 7. The reflector is made up of six components: back electrodes, a Plexiglas® mount, a conductive membrane, high-voltage power supplies, back-electrode connections, and front-electrode connections.

Reflector

Back Electrodes

The four back electrodes were fabricated using 0.032 Al and a paraboloidal mold. The Al was first cut into a circular disk of radius $9\frac{3}{4}$ in. and then sheared into four pieces. The four flat pieces were then placed in a paraboloidal mold and bent into shape. Because the four back electrodes are independently charged, they needed to be electrically isolated from each other. This isolation was accomplished by mounting the back electrodes onto a Plexiglas mount with a $\frac{3}{4}$-in. gap between them (Fig. 3, no. 5).

Plexiglas Mount

The Plexiglas mount was constructed using the same mold. First a $\frac{3}{8}$-in. sheet of acrylic was machined into a circular disk of radius $9\frac{3}{4}$ in. Then the acrylic was heated in a convection oven until it became pliable. Quickly removing the acrylic and inserting it into the cold male and female mold, compressing it, and letting it cool resulted in a finished Plexiglas mount (Fig. 3, no. 4). Each of the four back electrodes was secured to the Plexiglas mount using three number 4-40 machine screws.

Membrane Fabrication

The membrane, which is deformable and serves as the radiating surface, was constructed of 7-mil Lexan®. The process consisted of using a gasket cutter to cut the Lexan into a $9\frac{3}{4}$-in.-radius circular disk, heating the models up to 350°F in a convection oven, placing the Lexan in the mold, tightening down the bolts to 40 ft-lb, and allowing the unit to cool for 12 h. Once the Lexan was removed, it needed to be made conductive in the four regions matching the four back electrodes. This conductive application was performed by carefully masking the Lexan into four regions and painting it with a light coat of a conductive two-part epoxy paint. The paint gained its conductivity from the presence of carbon particles, which left the otherwise transparent Lexan with a flat black appearance on both sides. The top side of the membrane was given a light dusting of flat white paint to prepare its reflectivity for the optical sensor (Fig. 4, no. 8).

After being painted, the antenna membrane was secured above the Plexiglas mount by a number 2-56 threaded rod and some small nuts and washers (Fig. 1, no. 6). The Plexiglas mount was drilled and tapped in the center to fit the number 2-56 threaded rod. The nuts and washers suspended the antenna membrane $\frac{3}{4}$ in. above the Plexiglas mount.

Because the Lexan was only 7 mil thick, it sagged in the middle when placed on the threaded rod. The sagging was eliminated by placing a circular leafspringlike support under the membrane. The

Received 25 April 1997; revision received 22 January 1999; accepted for publication 30 January 1999.

*Mechanical and Aerospace Engineering; currently Project Manager, ERICSSON, 7001 Development Drive, Research Triangle Park, NC 27709.
†Professor, Mechanical and Aerospace Engineering.

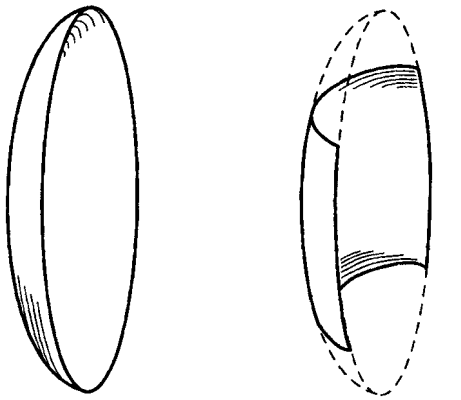

a) Full paraboloid b) Cut paraboloid

c) Parabolic cylinder

Fig. 1 Three forms of parabolic reflectors.

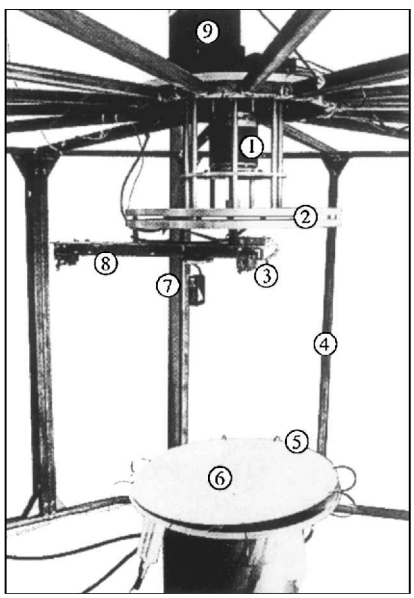

Fig. 2 Overview of setup: 1, motor for circumferential motion; 2, lazy susan; 3, motor for radial motion; 4, 1-in. box steel support structure; 5, antenna membrane; 6, number 2-56 threaded center post; 7, LED optical sensor; 8, linear positioner; and 9, power.

leafspringlike support was made out of three 7-mil Mylar® concentric disks of increasing radius ($r = 3$, 4, and 5 in.), which were heat formed into the paraboloidal shapes. Mylar was used instead of Lexan because of its relatively high stiffness.

High-Voltage Power Supply

Each back-electrode and front-electrode pair is controlled independently by a high-voltage power supply that delivers 0–30 kV at 0–1 mA. The charge passes from the power supplies to the back electrodes via high-voltage RG-8U coaxial cables (Fig. 4, no. 2). These cables are stiff and difficult to work with.

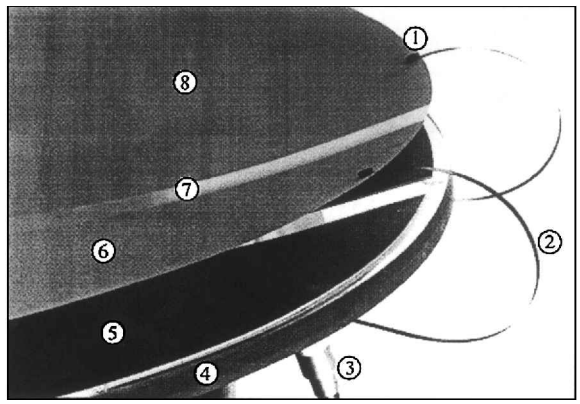

Fig. 3 Close-up of antenna membrane and back electrodes: 1, magnet; 2, conductive strip of Lexan; 3, PL259 uhf coaxial connector; 4, Plexiglas mount; 5, back electrode; 6, front electrode; 7, $\frac{3}{4}$-in. electrical discontinuity; and 8, antenna membrane.

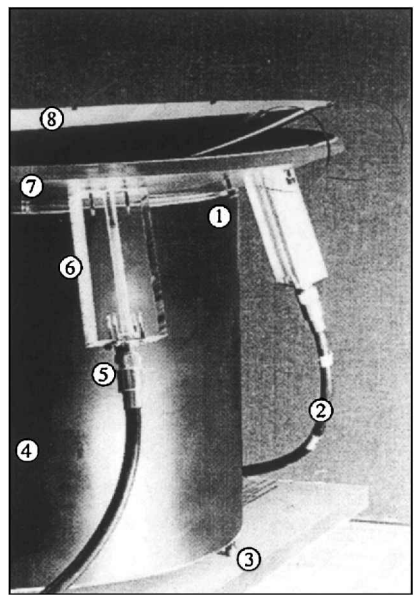

Fig. 4 Paraboloidally shaped antenna: 1, magnet; 2, RG-8/u coaxial cable; 3, leveling screw; 4, 13-in.-diam pvc; 5, PL259 and SO239 uhf connectors; 6, back-electrode coupling; 7, Plexiglas mount; and 8, antenna membrane.

Back-Electrode Coupling

The cables connect to the Plexiglas mount through the back-electrode couplings (Fig. 4, no. 6). Figure 5 is a close-up of one back-electrodecoupling. As shown, the coupling is a machined piece of 1-in.-thick rectangular acrylic. The end of the cable is fitted with a PL259 uhf connector, where the center conductor extends 4 in. past the point where the outer grounding sheath ends on the PL259 uhf. By knocking out the center on a SO239 uhf part and mounting it to the Plexiglas using four number 4-40 machine screws, it serves as a receptor for the PL259 uhf (Fig. 5, no. 5). The center conductor fits snugly, inside a hole drilled through the acrylic block (Fig. 5, no. 4). The acrylic block was attached to the Plexiglas mount with two number 6-32 machine screws (Fig. 5, no. 2). The hole in the block continues through the Plexiglas mount. A spring of appropriate length, placed in the hole before insertion of the center conductor, guarantees electrical continuity between the power supplies and the back electrodes (Fig. 5, no. 3). This complex arrangement prevents arcing between the grounded outer sheath and the high-voltage center conductor.

Back Electrodes to Front Electrodes

With the charge residing on the four back electrodes, the last step was to electrically pair the four front electrodes with the corresponding back electrodes. The main issue was to make the

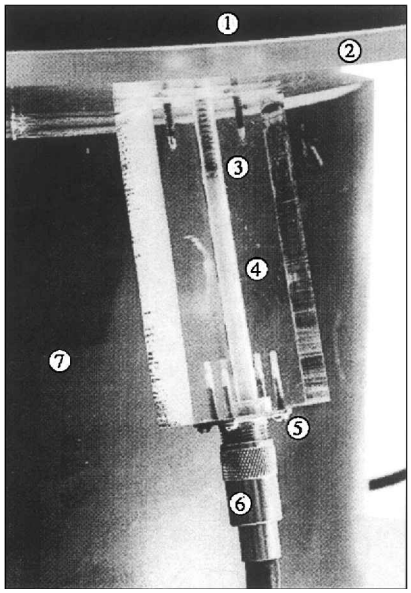

Fig. 5 Close-up of back-electrode coupling: 1, bottom of antenna membrane; 2, Plexiglas mount; 3, spring; 4, hole through acrylic block; 5, PL259 uhf receptor; 6, SO239 uhf connector; and 7, 13-in.-diam pvc.

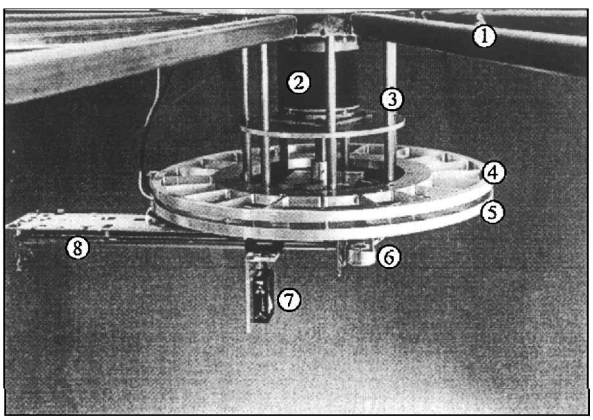

Fig. 6 Cylindrical measurement device: 1, 1-in. box steel support structure; 2, motor for circumferential motion; 3, vertical suspension rods; 4, lazy susan top; 5, lazy susan bottom; 6, motor for radial motion; 7, LED optical sensor; and 8, linear positioner.

connections without interfering with the membrane's freedom of motion. Figure 3, no. 1, shows the solution. A sheet of 5-mil Lexan was painted with conductive epoxy on one side. Then eight thin strips 7 in. long and $\frac{1}{8}$ in. wide were cut using a plate of glass, a steel scale, and a utility knife (Fig. 3, no. 2). By connecting one side of the strip to the front electrode and the other side of the strip to the back electrode mounting screw that protrudes through the bottom of the Plexiglas mount, a nonintrusive conductive connection was accomplished. (Conductive adhesives could also have been used but were ruled out because of the expense.) Ultrastrong neodymium iron boron magnets of $\frac{1}{8}$ in. diameter and $\frac{1}{16}$ in. thickness with a 1-lb lift force were used to secure the conductive strip. Two magnets were used to sandwich the front electrode and electrical contact strip together (Fig. 3, no. 1). A steel nut threaded onto the tip of the mounting screw and a single magnet were used to sandwich the back electrode and the electrical contact strip. The steel nut created a flat contact surface, and the mounting screw needed to be nonferrous to avoid its attraction to the front-electrode magnets.

Measurement System

The components of the cylindrical measurement device are: a proximity sensor, a linear positioner, an angular positioner, and a computer.

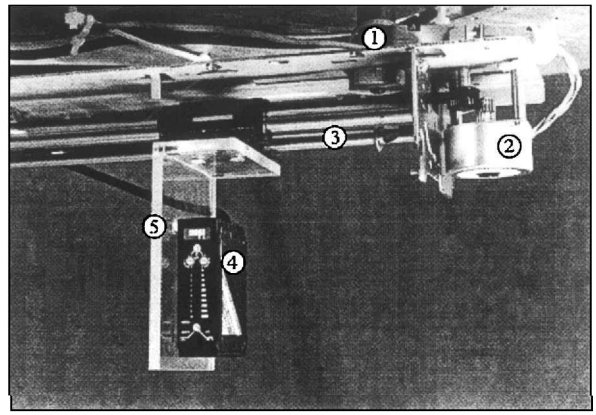

Fig. 7 Linear positioner: 1, circumferential motor shaft; 2, motor for radial motion; 3, radial guide rods; 4, LED optical sensor; and 5, sensor carriage.

Components

Sensor

The proximity sensor is a light-emitting diode (LED) optical sensor that determined distance through triangulation (Fig. 6, no. 7). The analog output of 0–5 V is proportional to distance. This output signal was calibrated using a linear positioner attached to a high-precision steel scale. The mapping of the membrane used a linear positioner for translation in the radial direction and an angular positioner for rotation in the circumferential direction.

Linear Positioner

The linear positioner holds the sensor, which in turn is mounted on a carriage that is guided by radially directed rods. The carriage is actuated by a stepper motor, some gears, and a belt (Fig. 7).

Angular Positioner

The linear positioner device just described is mounted on the angular positioner. The angular positioner is actuated by a large second stepper motor, as shown in Fig. 6, no. 2.

Data Acquisition System

The position of the sensor and the recording of its output was performed by a Macintosh IIci personal computer using Labview software and two nu-bus cards (NB MIO-16 and NB AO-6).

Test Cases

To test the antenna's ability to both point and bend, 11 different cases were developed. Figure 8 diagrams the eight test cases associated with pointing. Pointing is defined as the rigid-body rotation of the antenna. It is measured relative to the static equilibrium. The selection of test cases considers the need to avoid voltage feedover between adjacent electrodes. Voltage feedover is an event that occurs when a high-voltage electrode starts to effect a lower one, which in turn can damage power supplies.[4] In this experiment, the gap between adjacent electrodes was $\frac{3}{4}$ in., and voltage feedover was experimentally found to occur at voltage differences in excess of 15 kV. The maximum voltage difference between adjacent electrodes was limited to 10 kV, allowing for a 1.5 factor of safety.

Based on a simple interpretation of Coulomb's law, the nth test case is expected to rotate the surface reflector about an axis that is located in the xy plane and oriented at $\theta = 45(n-1)$ deg relative to the x axis. With 10 test cases we can demonstrate pointing about principle axes and about axes that are 45 deg from the principle axes.

To help further explain these two criteria, we examine test case 2. Test case 2 applies 25 kV to electrode pair I, 15 kV to electrode pair II, 5 kV to electrode pair III, and 15 kV to electrode pair IV (Fig. 8). The first test criterion is satisfied with a maximum difference between adjacent electrode pairs of 10 kV. Notice that the difference between electrode pairs I and II is 20 kV, which is acceptable because they are not adjacent. The second criterion indicates that electrode pair I is 1.66 times greater than II and IV and 5 times greater than III. Predicting the motion of the reflector surface, one

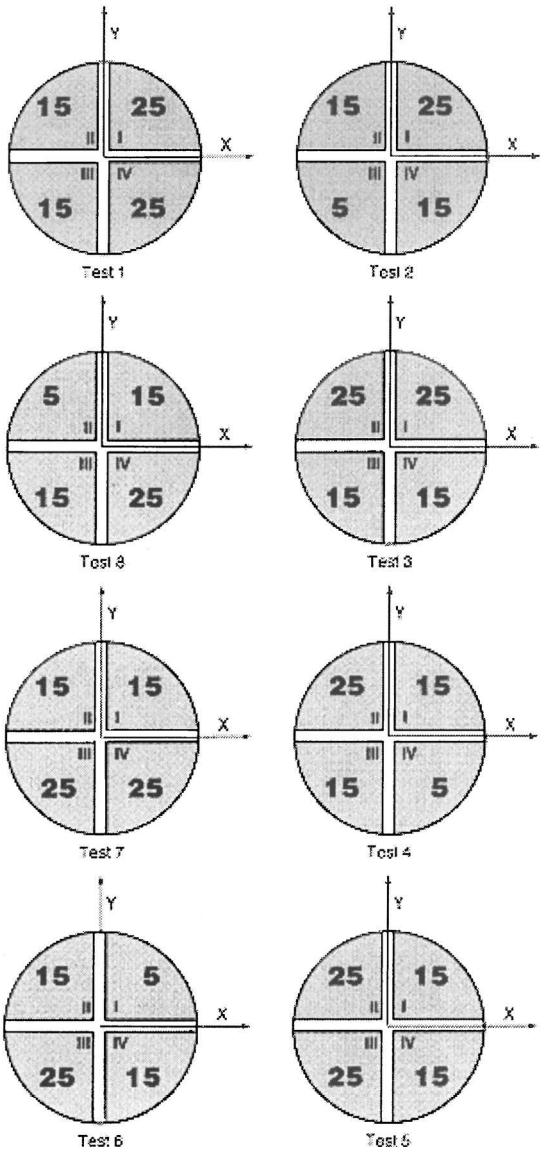

Fig. 8 Eight pointing test cases as seen from above; each quadrant is charged to the specified value in kilovolts.

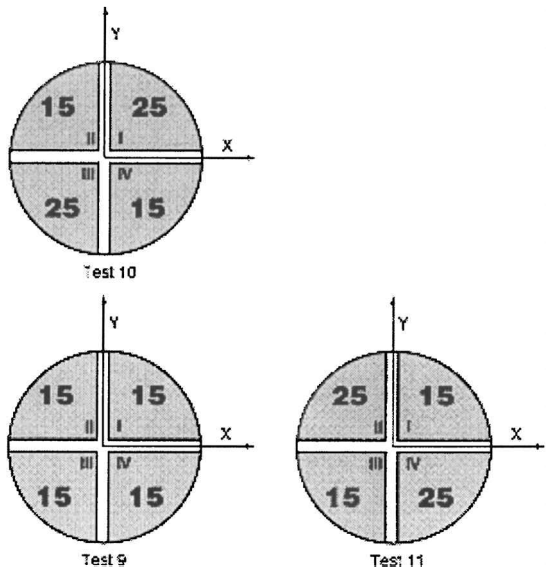

Fig. 10 Two bending test cases and the nominal test case; each quadrant is charged to the specified value in kilovolts.

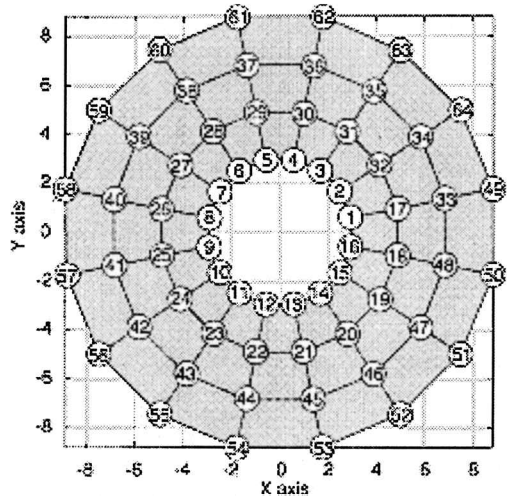

Fig. 11 Location of the 64 surface measurements.

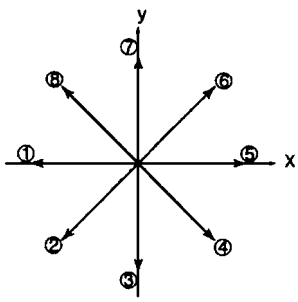

Fig. 9 Representation of which way the antenna should point for the eight test cases.

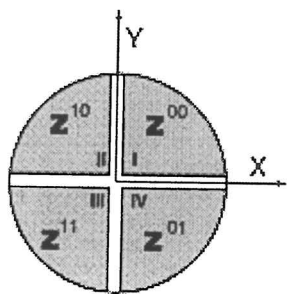

Fig. 12 Values of z in the different quadrants as defined by the different double indices.

would expect to see a rotation about the $y = -x$ line. This corresponds to a direction angle of $\theta = 225$ deg. Figure 9 shows the desired direction of test cases 1–8. The lines indicate which direction the antenna should point.

Figure 10 maps out two bending test cases and the nominal case. Bending is accomplished by applying identical charges to electrode pairs that are diagonal to each other. For example, electrode pair I must be at the same voltage as III, and II must be at IV for bending to work. Because there are only four electrode pairs, there are only two ($\frac{4}{2} = 2$) bending test cases. The magnitude of bending was maximized, while adhering to the first criterion.

The nominal test case (9) in which all four electrodes are charged to 15 kV was used as a baseline.

Sixty-Four Measurement Positions

Four concentric circles of increasing radius ($r = 3, 5, 7$, and 9 in.) were discretized into 16 points, one every 22.5 deg, resulting in a total of 64 data points for each test case (Fig. 11). Then a double index was assigned to the collected data (Fig. 12). This double index assignment was done for the purpose of determining rotation angles θ_x and θ_y. We first consider two rotation matrices associated with

an arbitrary point (x, y, z), given by

$$\begin{Bmatrix} x_n \\ y_n \\ z_n \end{Bmatrix} = \begin{bmatrix} \cos(\theta_y) & 0 & \sin(\theta_y) \\ 0 & 1 & 0 \\ -\sin(\theta_y) & 0 & \cos(\theta_y) \end{bmatrix} \begin{Bmatrix} x \\ y \\ z \end{Bmatrix}$$

$$\begin{Bmatrix} x_n \\ y_n \\ z_n \end{Bmatrix} = \begin{bmatrix} 1 & 0 & 0 \\ 0 & \cos(\theta_x) & -\sin(\theta_x) \\ 0 & \sin(\theta_x) & \cos(\theta_x) \end{bmatrix} \begin{Bmatrix} x \\ y \\ z \end{Bmatrix} \tag{1}$$

Combining the two yields the transformation

$$\begin{Bmatrix} x_n \\ y_n \\ z_n \end{Bmatrix} = \begin{bmatrix} \cos(\theta_y) & 0 & \sin(\theta_y) \\ 0 & 1 & 0 \\ -\sin(\theta_y) & 0 & \cos(\theta_y) \end{bmatrix} \begin{bmatrix} 1 & 0 & 0 \\ 0 & \cos(\theta_x) & -\sin(\theta_x) \\ 0 & \sin(\theta_x) & \cos(\theta_x) \end{bmatrix} \begin{Bmatrix} x \\ y \\ z \end{Bmatrix}$$

$$= \begin{bmatrix} \cos(\theta_y) & \sin(\theta_y)\sin(\theta_x) & \sin(\theta_y)\cos(\theta_x) \\ 0 & \cos(\theta_x) & -\sin(\theta_x) \\ -\sin(\theta_y) & \cos(\theta_y)\sin(\theta_x) & \cos(\theta_y)\cos(\theta_x) \end{bmatrix} \begin{Bmatrix} x \\ y \\ z \end{Bmatrix} \tag{2}$$

The rotation angles θ_x and θ_y in Eq. (2) are determined by minimizing the average rotation of the transformed points (x_n, y_n, z_n), as described later. Next, we pair the quadrants. We let $1 < i < p$, where $p = 16$, and let the vertical position of the ith point in the (j, k)th quadrant be denoted by (see Fig. 12)

$$z_i^{jk} = \left((-1)^j x_p (-1)^k y_i\right) \tag{3}$$

with the need to change p to i, and we let

$$z_i^{00} = (x_i, y_i) \tag{4a}$$

$$z_i^{10} = (-x_i, y_i) \tag{4b}$$

$$z_i^{11} = (-x_i, -y_i) \tag{4c}$$

$$z_i^{01} = (x_i, -y_i) \tag{4d}$$

The vertical position in the new coordinate system is obtained from the last row of Eq. (2) after making a small-angle approximation:

$$z_{ni} = \theta_x y_i - \theta_y x_i + z_i \tag{5}$$

In each of the quadrants we have

$$z_{ni}^{00} = \theta_x y_i - \theta_x x_i + z_i^{00} \tag{6a}$$

$$z_{ni}^{10} = \theta_x y_i + \theta_y x_i + z_i^{10} \tag{6b}$$

$$z_{ni}^{11} = -\theta_x y_i + \theta_y x_i + z_i^{11} \tag{6c}$$

$$z_{ni}^{01} = -\theta_x y_i - \theta_y x_i + a_i^{01} \tag{6d}$$

We now define the error functions

$$E_x = \sum_{i=1}^{p} \left[\left(z_{ni}^{00} - z_{ni}^{01}\right)^2 + \left(z_{ni}^{10} - z_{ni}^{11}\right)^2 \right] \tag{7a}$$

$$E_y = \sum_{i=1}^{p} \left[\left(z_{ni}^{00} - z_{ni}^{10}\right)^2 + \left(z_{ni}^{01} - z_{ni}^{11}\right)^2 \right] \tag{7b}$$

Substituting Eqs. (6) into Eq. (7a), we get

$$E_x = \sum_{i=1}^{p} \left[\left(2\theta_x y_i + z_i^{00} - z_i^{01}\right)^2 + \left(2\theta_x y_i + z_o^{10} - z_i^{11}\right)^2 \right] \tag{8}$$

Equation (8) expresses the error function explicitly in terms of the rotation angle θ_x. Differentiating with respect to θ_x yields

$$\frac{dE_x}{d\theta_x} = \sum_{i=1}^{p} \left[2\left(2\theta_x y_i + z_i^{00} - z_i^{01}\right)2y_i + 2\left(2\theta_x y_i + z_i^{10} - z_i^{11}\right)2y_i \right] \tag{9}$$

By letting $dE_x/d\theta_x = 0$, we get the rotation angle

$$\theta_x = \frac{\sum_{i=1}^{p} \left(z_i^{00} + z_i^{10} - z_i^{01} - z_i^{11}\right) y_i}{4\left(\sum_{i=1}^{p} y_i^2\right)} \tag{10}$$

We determine the rotation angle θ_y following the same steps and get

$$\theta_y = \frac{\sum_{i=1}^{p} \left(z_i^{00} + z_i^{01} - z_i^{10} - z_i^{11}\right) x_i}{4\left(\sum_{i=1}^{p} x_i^2\right)} \tag{11}$$

The surface deformations are determined by

$$\Delta z(x, y) = z_{\text{test case}}(x, y) - z_{\text{nominal}}(x, y) \tag{12}$$

This equation needs to be changed back. The values of Δz depend on position and are expressed as polynomials in the form

$$\Delta z(x, y) = a_0 + a_1 x + a_2 y + a_3 xy + a_4 x^2 + a_5 y^2 + a_6 xy^2 + a_7 x^2 y + a_8 x^3 + a_9 y^3 \tag{13}$$

Writing Eq. (13) in matrix form gives

$$\begin{Bmatrix} \Delta z(1) \\ \Delta z(2) \\ \vdots \\ \Delta z(64) \end{Bmatrix} = \begin{bmatrix} 1 & x_1 & y_1 & x_1 y_1 & x_1^2 & y_1^2 & x_1 y_1^2 & x_1^2 y_1 & x_1^3 & y_1 3 \\ 1 & x_2 & y_2 & x_2 y_2 & x_2^2 & y_2^2 & x_2 y_2^2 & x_2^2 y_2 & x_2^3 & y_2^3 \\ \vdots & \vdots & \vdots & \vdots & \vdots & \vdots & \vdots & \vdots & \vdots & \vdots \\ 1 & x_{64} & y_{64} & x_{64} y_{64} & x_{64}^2 & y_{64}^2 & x_{64} y_{64}^2 & x_{64}^2 y_{64} & x_{64}^3 & y_{64}^3 \end{bmatrix} \begin{Bmatrix} a_0 \\ a_1 \\ \vdots \\ a_9 \end{Bmatrix} \tag{14}$$

for the 64 measurement points, resulting in the linear equation

$$\boldsymbol{z} = \boldsymbol{C}\boldsymbol{a} \tag{15}$$

The coefficients $\boldsymbol{a}$ in Eq. (15) are determined from the least-squares solution

$$\boldsymbol{a} = (\boldsymbol{C}^T \boldsymbol{C})^{-1} \boldsymbol{C}^T \boldsymbol{z} \tag{16}$$

Coefficients a_0–a_9 are given in Tables 1 and 2. The coefficients a_0–a_9 depend on the applied voltages V_1, V_2, V_3, and V_4. By the assuming a polynomial of the form

$$a_r(v) = b_r + c_r^T v + v^T D_r v \tag{17}$$

where $r = 0, 1, 2, \ldots, 9$ and $v = (V_1, V_2, V_3, V_4)^T$, we determine another least-squares solution, resulting in the coefficients given in Tables 3 and 4. By using Eqs. (15) and (17), Tables 1–4, and a given set of applied voltages, the surface deflection at any point is predicted.

Table 1 Coefficients a_0–a_9 for test cases 1–5

Coefficient	Test case 1	Test case 2	Test case 3	Test case 4	Test case 5
a_0	7.9681e−03	4.0645e−03	4.7706e−03	6.6205e−03	1.0573e−02
a_1	6.0645e−05	−1.9352e−03	−4.5922e−03	−6.2749e−03	−2.8258e−03
a_2	−2.0603e−03	1.4775e−02	2.4532e−02	2.4451e−02	1.0389e−02
a_3	1.2373e−04	3.8319e−04	7.2906e−05	−2.4401e−04	1.0901e−04
a_4	−7.1925e−05	6.7407e−05	3.8819e−05	−2.3770e−04	−1.9122e−04
a_5	−1.0000e−04	−2.7803e−04	−2.0997e−04	1.5066e−04	2.3305e−04
a_6	8.1213e−05	4.0073e−05	1.3319e−05	−1.8826e−05	−6.1496e−05
a_7	1.4362e−06	6.2924e−05	4.9245e−05	1.2853e−05	−1.6090e−05
a_8	1.7187e−05	2.8764e−05	4.3791e−05	5.3575e−05	1.2883e−05
a_9	−1.3182e−05	−4.6069e−06	9.5362e−06	4.5537e−05	2.7390e−05

Table 2 Coefficients a_0–a_9 for test cases 6–8, 10, and 11

Coefficient	Test case 6	Test case 7	Test case 8	Test case 10	Test case 11
a_0	9.3381e−03	4.5367e−03	−1.2480e−03	−2.3244e−03	−2.6482e−03
a_1	9.3614e−04	1.8200e−03	2.4816e−03	−6.6065e−04	−1.4640e−03
a_2	−9.1976e−03	−2.0662e−02	−1.7397e−02	−2.4477e−03	3.0491e−03
a_3	2.9963e−04	−8.5181e−05	−2.9396e−04	9.2318e−04	−8.1754e−04
a_4	2.7873e−05	1.6763e−04	4.9744e−05	2.0231e−04	−1.5364e−04
a_5	−2.2978e−05	−2.2113e−04	−1.0583e−04	−1.4237e−04	1.4997e−04
a_6	−4.9747e−05	−8.8797e−06	2.9319e−05	3.6393e−06	3.4282e−06
a_7	−5.7412e−05	−5.0300e−05	−5.4295e−05	−6.3146e−06	−2.4043e−05
a_8	−2.0514e−05	−1.4109e−07	3.5688e−06	9.1260e−08	1.9050e−05
a_9	2.5344e−05	2.6644e−05	−5.3614e−06	2.8057e−05	1.0135e−05

Table 3 Coefficients b_r, c_r, and D_r for a_0–a_4

Coefficient	a_0	a_1	a_2	a_3	a_4
b	−2.3449e−07	−1.6988e−08	8.2306e−08	2.7250e−10	2.0415e−10
c_1	−3.5151e−04	−2.2847e−05	−5.7883e−05	−4.5884e−06	4.6716e−06
c_2	5.7196e−04	−1.7481e−04	−1.3773e−04	−5.7686e−06	−1.0137e−05
c_3	3.4756e−04	2.2558e−05	5.9302e−05	4.6207e−06	−4.6626e−06
c_4	−5.7592e−04	1.7809e−04	1.3917e−04	5.7465e−06	1.0135e−05
d_{11}	−9.6354e−06	−3.6105e−07	1.6883e−05	1.4476e−06	2.4318e−07
d_{12}	1.0370e−05	−1.0053e−06	8.3566e−06	−1.8734e−07	5.1054e−07
d_{13}	−2.8918e−05	−1.3402e−07	−2.1961e−06	−2.2590e−07	5.6341e−08
d_{14}	3.9742e−05	−3.1002e−07	−2.4082e−07	3.0843e−07	−7.1262e−07
d_{21}	1.0370e−05	−1.0053e−06	8.35676e−06	−1.8734e−07	5.1054e−07
d_{22}	−2.9791e−05	−42155e−06	2.7883e−05	−1.1608e−06	−2.2278e−07
d_{23}	2.9826e−05	−1.6969e−07	8.5382e−06	3.1364e−07	−6.0213e−07
d_{24}	−1.9083e−05	2.8568e−06	−3.6661e−06	2.1247e−07	1.8799e−07
d_{31}	−2.8918e−05	−1.3402e−07	−2.1961e−06	−2.2590e−07	5.6341e−08
d_{32}	−2.9826e−05	−1.6969e−07	−8.5382e−06	3.1364e−07	−6.0213e−07
d_{33}	−1.6892e−05	1.2750e−06	−5.0476e−06	1.2245e−06	3.6581e−07
d_{34}	1.3029e−05	4.9038e−07	−2.2353e−05	−4.1567e−07	5.2268e−07
d_{41}	3.9742e−05	−3.1002e−07	−2.4082e−07	3.0843e−07	−7.1262e−07
d_{42}	−1.9083e−05	2.8568e−06	−3.6661e−06	2.1247e−07	1.8799e−07
d_{43}	1.3029e−05	4.9038e−07	−2.2353e−05	−4.1567e−07	5.2268e−07
d_{44}	−1.7216e−05	−2.8601e−06	−1.1605e−05	−1.3943e−06	−3.2112e−07

Table 4 Coefficients b_r, c_r, and D_r for a_5–a_9

Coefficient	a_5	a_6	a_7	a_8	a_9
b	9.5396e−10	−2.7451e−10	−7.6605e−10	1.1316e−10	7.1088e−10
c_1	−1.3578e−06	−3.3884e−06	3.2468e−06	1.3110e−06	1.3372e−06
c_2	−1.5656e−07	4.2215e−06	5.5669e−07	2.0297e−06	3.3360e−06
c_3	1.3691e−06	3.3838e−06	−3.2597e−06	−1.3092e−06	−1.3246e−06
c_4	1.7694e−07	−4.2261e−06	−5.7009e−07	−2.0273e−06	−3.3240e−06
d_{11}	−3.2065e−07	5.9900e−08	−3.1956e−08	−2.6587e−08	1.8054e−08
d_{12}	−8.5854e−07	−4.3254e−09	6.4183e−08	2.3828e−08	−3.6243e−08
d_{13}	3.4998e−07	1.3214e−08	−4.0135e−08	−5.6699e−09	2.1012e−08
d_{14}	4.4218e−07	1.2433e−07	1.1598e−08	2.8512e−09	−5.6881e−08
d_{21}	−8.5854e−07	−4.3254e−09	6.4183e−08	2.3828e−08	−3.6243e−08
d_{22}	4.8750e−07	−9.9339e−08	−7.9056e−08	3.4706e−08	3.1522e−08
d_{23}	6.3538e−07	−5.9991e−08	3.4267e−08	−8.8191e−09	−5.6512e−08
d_{24}	1.0033e−07	−1.2127e−08	7.4811e−09	−5.4942e−08	−1.4484e−08
d_{31}	3.4998e−07	1.3214e−08	−4.0135e−08	−5.6699e−09	2.1012e−08
d_{32}	6.3538e−07	−5.9991e−08	3.4267e−08	−8.8191e−09	−5.6512e−08
d_{33}	−1.5356e−07	−1.2782e−07	−2.3794e−08	−2.3982e−08	8.7376e−08
d_{34}	−8.8465e−07	−7.7284e−09	4.9676e−08	3.8103e−08	3.2711e−08
d_{41}	4.4218e−07	1.2433e−07	1.1598e−08	2.8512e−09	−5.6881e−08
d_{42}	1.0033e−07	−1.2127e−08	7.4811e−09	−5.4942e−08	−1.4484e−08
d_{43}	−8.8465e−07	−7.7284e−09	4.9676e−08	3.8103e−08	3.2711e−08
d_{44}	2.6820e−07	8.1574e−08	−1.1623e−07	6.0651e−08	1.0011e−07

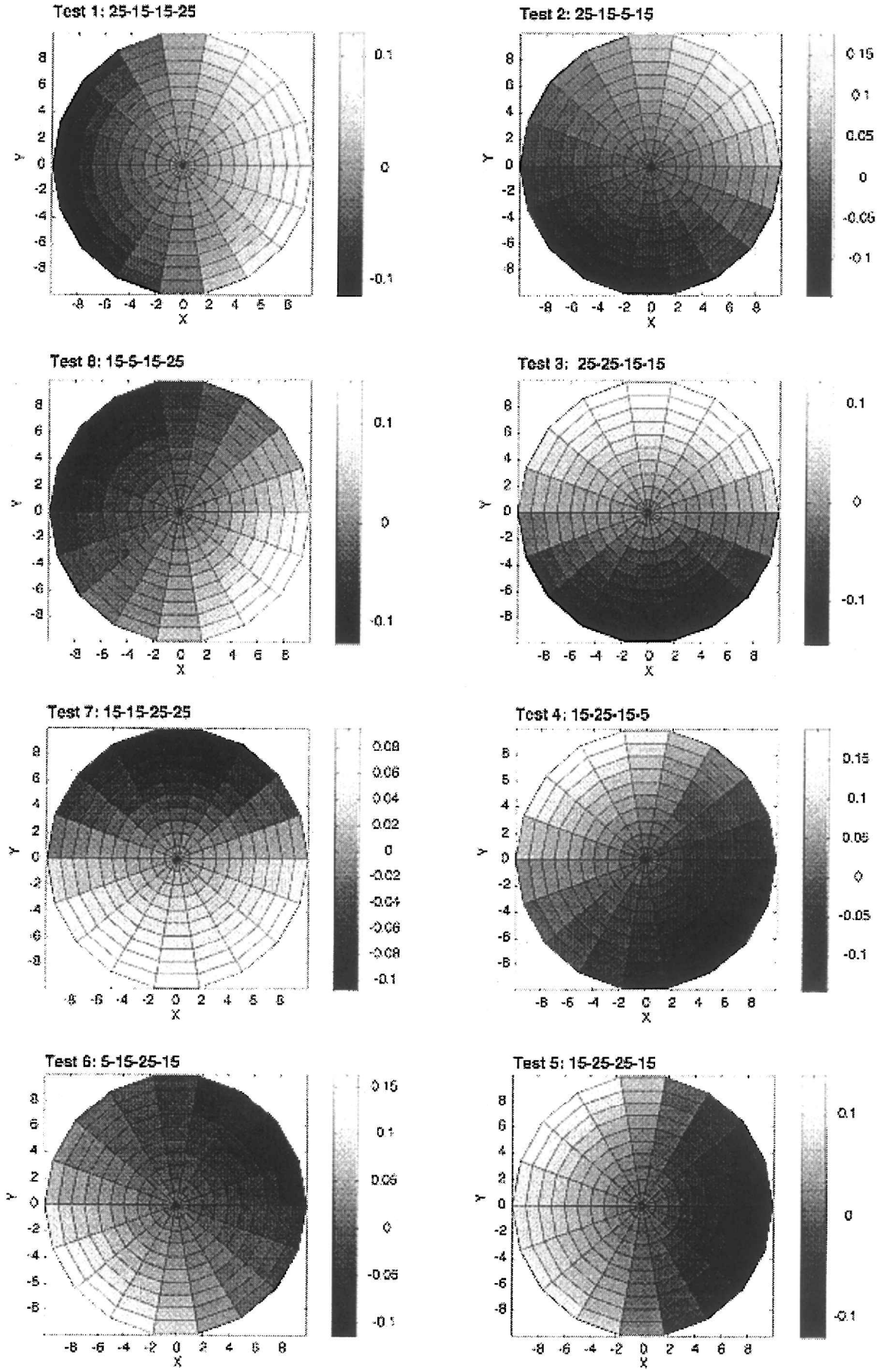

Fig. 13 Contour plots of the eight pointing test cases, where light areas indicate a rise in the antenna and the dark areas a decrease.

Results and Discussion

Figure 13 shows the surface reflector's deflections in the form of contour plots. The light areas indicate positive surface deformations, and the dark areas indicate negative. Comparing the reflector surfaces predicted direction of rotation, given in Fig. 9, to the contour plots, given in Fig. 13, one finds strong correlation between the two. Test case 2, for example, was predicted to point in a direction corresponding to 225 deg. Figure 13 (test 2) shows just that. The darkest area is in quadrant III and the lightest area is in quadrant I. This indicates a rotation about the $y = -x$ axis.

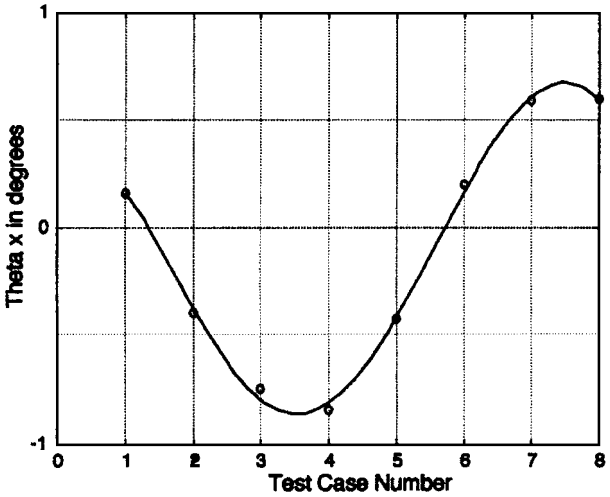

Fig. 14 Rotation about the x axis in degrees vs the test case number.

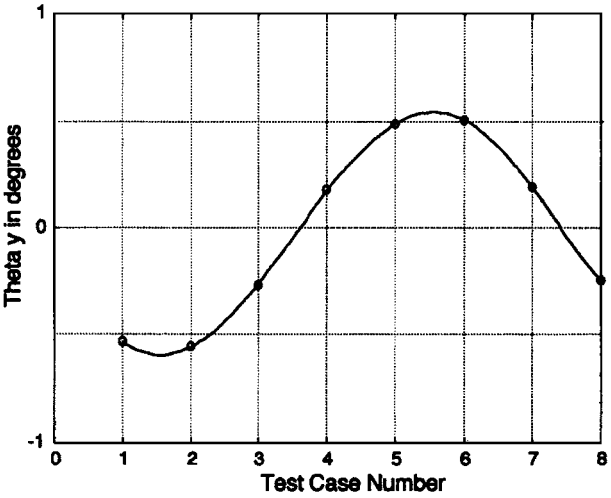

Fig. 15 Rotation about the y axis in degrees vs the test case number.

Table 5 Rotation about the x and y axes for each different test case, in degrees

Test case	θ_x	θ_y
1	0.1607	−0.5311
2	−0.3921	−0.5486
3	−0.7447	−0.2667
4	−0.8436	0.1778
5	−0.4215	0.4842
6	0.1980	0.4976
7	0.5902	0.1885
8	0.5957	−0.2471

On average, the edge of the surface reflector displaced $\frac{1}{4}$ in. This corresponds to an angular rotation of $\frac{6}{10}$ deg. The individual rotations about the x and y axes are given in Table 5. Figures 14 and 15 show the rotation angles θ_x and θ_y vs the respective test case. A fourth-order polynomial fit is performed and plotted over the θ_x and θ_y values. The resulting out-of-phase sine functions further show the surface reflector's pointing capabilities.

The results of the bending test cases are also presented as contour plots in Fig. 16. Maximum edge deflections are on the order of $\frac{1}{10}$ in., which is lower than the pointing test cases. These smaller deflections are attributed to the higher energy level needed to deform the surface reflector in its second mode. The surface performed as expected, bending about the $y = -x$ axis in test case 10 and about the $y = x$ axis in test case 11.

Sources of Error

Ideally, the reflector should have had maximum and minimum angles of rotation that were identical in magnitude. Table 5 shows close but not perfect compliance with this charge. Theoretically, test cases 1 and 5 should have had zero rotation about the x axis and θ_y should have been equal in magnitude for both cases. In actuality θ_x differed by 0.5822 deg and θ_y by 0.0469 deg. Thus, while θ_x varied by half a degree, θ_y was an order of magnitude closer to the ideal. There are five main reasons for the error: First and foremost, the Lexan has directional in-plane stiffness. Second, after heat forming the Lexan into shape, the plastic was found to vary between 6.5 and 7 mil. Third, even though great care was taken to spray the paints as uniformly as possible, weight variations existed. Fourth, the magnets and conductive strips used to charge the front electrodes introduced weight imbalances and localized stiffness to the surface reflector. Fifth, edge alignment between front electrodes and back electrodes is important because that charge concentrates along them. Deviations can result in disproportionate magnitudes of push.

Conclusion

The surface of a full paraboloidally shaped reflector was recon figured using electrostatic forces of repulsion. A set of test cases demonstrated the pointing and beam-width control of the radiation surface. The surface reflector angles of rotation θ_x and θ_y were plotted vs eight test cases. The resulting sine functions show the

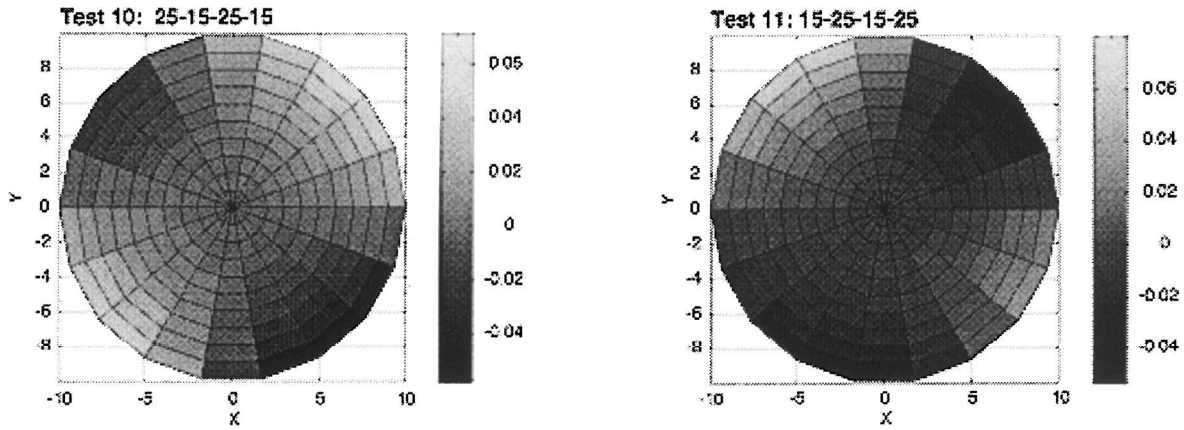

Fig. 16 Contour plots of the two bending test cases, where light areas indicate a rise in the antenna membrane and the dark areas a decrease.

near-linear relationship between voltage and pointing, indicating that expected rotations are in agreement with measurements and that a simple interpretation of Coulomb's law dominates the behavior of the system.

Acknowledgments

This work was supported in part by the Mars Mission Research Center, NASA Grant NAGW-1331, and the North Carolina Space Grant Consortium, NASA Grant NGT5-40011.

References

[1]Silverberg, L., and Stanley, R. J., "Space-Based Electrostatic Antenna Design with Pointing and Beam Width Control," *Journal of Spacecraft and Rockets*, Vol. 33, No. 6, 1996, pp. 843–847.

[2]Silverberg, L., and Washington, G., "Modal Control of Reflector Surfaces Using Far-Field Power Measurements," *Microwave and Optical Technology Letters*, Vol. 7, No. 12, 1994, pp. 588–593.

[3]Washington, G., and Silverberg, L., "Modal Control of a Corner Reflector to Maximize Far-Field Power," *Microwave and Optical Technology Letters*, Vol. 8, No. 5, 1995, pp. 260–264.

[4]Goslee, J. W., and Hinson, W. F., "Measurement of Electrostatically Formed Antennas Using Photogrammetry and Theodolites," American Congress on Surveying and Mapping, Washington, DC, March 1984.

I. E. Vas
Associate Editor